Taylor & Francis Taylor & Francis Group

Heat Transfer Engineering

ISSN: (Print) (Online) Journal homepage: https://www.tandfonline.com/loi/uhte20

Investigation of critical heat flux enhancement on nanoengineered surfaces in pressurized subcooled flow boiling using infrared thermometry

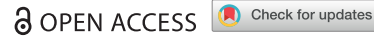
Chi Wang, Guanyu Su, Olorunsola Akinsulire, Limiao Zhang, Md Mahamudur Rahman & Matteo Bucci

To cite this article: Chi Wang, Guanyu Su, Olorunsola Akinsulire, Limiao Zhang, Md Mahamudur Rahman & Matteo Bucci (28 Mar 2023): Investigation of critical heat flux enhancement on nanoengineered surfaces in pressurized subcooled flow boiling using infrared thermometry, Heat Transfer Engineering, DOI: 10.1080/01457632.2023.2191441

To link to this article: https://doi.org/10.1080/01457632.2023.2191441

9	© 2023 The Author(s). Published with license by Taylor & Francis Group, LLC
	Published online: 28 Mar 2023.
	Submit your article to this journal $oldsymbol{\mathcal{Z}}$
ılıl	Article views: 902
ď	View related articles 🗷
CrossMark	View Crossmark data ☑







Investigation of critical heat flux enhancement on nanoengineered surfaces in pressurized subcooled flow boiling using infrared thermometry

Chi Wang^a, Guanyu Su^a, Olorunsola Akinsulire^a, Limiao Zhang^a, Md Mahamudur Rahman^{a,b}, and Matteo Buccia

^aDepartment of Nuclear Science and Engineering, Massachusetts Institute of Technology, Cambridge, Massachusetts, USA; ^bDepartment of Mechanical Engineering, University of Texas at El Paso, El Paso, Texas, USA

ABSTRACT

Enhancing the flow boiling critical heat flux (CHF) is beneficial to the economics and safety margins of many industrial applications cooled by boiling heat transfer. While many studies have shown that surfaces with hydrophilic nanoscale and micro-scale features can enhance CHF in pool boiling, it is still not clear how these engineered surfaces affect the CHF in subcooled flow boiling at ambient pressure, let alone high-pressure conditions. Here, two nanoengineered surfaces, i.e., a surface coated with a porous layer of hydrophilic silica nanoparticles and a surface coated with zinc oxide nanowires, were tested. Flow boiling tests with a 10 K subcooling and a mass flux of 1000 kg/(m²·s) were conducted at 1 bar and 4 bars using infrared thermometry diagnostics. At 1 bar, the CHF enhancement is around 15% for both coatings. At 4 bars, the CHF enhancement is around 17% for the nanowire surface, and around 25% for the nano-porous surface. Infrared thermometry measurements reveal that the CHF enhancement comes from an increase of both two-phase heat transfer and single-phase heat transfer mechanisms, which is due to a change of bubble dynamics on the nanoengineered surfaces. It is also shown that the boiling crisis can be predicted using a percolation model based on Monte Carlo (MC) simulations.

Introduction

Flow boiling is used to remove heat in a variety of industrial applications, the size of which can be as small as an electronic chip, or as large as a nuclear reactor. One limiting factor for flow boiling heat transfer is the critical heat flux (CHF), defined as the heat flux at which a boiling crisis occurs. When the heat flux is below the CHF, the boiling process is in the nucleate boiling regime and discrete, non-interacting bubbles nucleate on the boiling surface. Such heat transfer regime is very effective, i.e., high heat fluxes can be removed with a relatively low surface temperature compared to single-phase forced convection. However, if the heat flux exceeds the CHF, the boiling regime changes into a film boiling regime. In film boiling, a stable vapor patch isolates the heated surface. The existence of the vapor film severely deteriorates the efficiency of the heat transfer process and may result in a catastrophic rise of the surface temperature (e.g., the surface to be cooled may melt down). As a

result, the operating heat flux of industrial applications cooled by nucleate boiling is set to be much lower than the CHF limit to avoid the boiling crisis and ensure safe and continuous operation. Still, in systems where boiling is used for cooling purposes, e.g., nuclear reactors, a higher operating heat flux is often beneficial, as it leads to a better economic efficiency or a larger safety margin.

Studies have been carried out for over half a century to understand the physics of the boiling crisis and enhance the CHF limits. Recent studies with super hydrophilic nano-engineered surfaces have shown promising results in pool boiling, using different surface engineering strategies, such as nanowires [1-4], nano-porous layers [5-7], carbon nanotubes [8], microscale pillars [9-12] and cavities [13], microscale ridges [14] and other microscale and nanoscale features [15–18]. However, while there are many works on flow boiling in micro-channels at relative low pressure [19, 20] and a few studies of flow boiling in macro-channels studying accident-tolerant fuel nuclear

Technology, Cambridge, Massachusetts 02139, USA



CONTACT Associate Professor Matteo Bucci ambucci@mit.edu Department of Nuclear Science and Engineering, Massachusetts Institute of

Nomenclature									
A _{heat} a _{micro} CHF f G	active heating surface area, m ² microlayer covered area, m ² critical heat flux bubble frequency, Hz giant cluster gravity constant, m/s ²	$\begin{array}{c} t_q \\ U \\ V_0'' \\ Wi \\ W_r \end{array}$	elapsed time, s measured voltage, V measured initial volumetric flux, m/s wicking number microlayer ring width, m						
g hq I IR ITO K MC N" PDF q"	transient conduction heat transfer coefficient, W/(m²·K) measured current, A infrared indium tin oxide influence area factor Monte Carlo nucleation site density, 1/m² probability density function heat flux, W/m²		liquid thermal effusivity, W _{\s} /(m ² ·K) critical filling factor fluid viscosity, Pa·s instantaneous bubble density, 1/m ² departure bubble density, 1/m ² liquid density, kg/m ³ vapor density, kg/m ³ surface tension, N/m						
$\begin{array}{l} q_{CHF,e}''\\ q_{CHF,p}''\\ q_{Quench}''\\ R\\ < R> \\ r_{dep}\\ SEM\\ SG\\ T_b\\ T_{wall}\\ t_w\\ t_g \end{array}$	CHF on engineered surface, W/m ² CHF on plain surface, W/m ² quenching heat flux, W/m ² radius, m average radius, m departure bubble radius, m scanning electron microscope second giant cluster bulk temperature, °C wall temperature, °C wait time, s growth time, s	Subscript CHF,e CHF,p c dep g l q r	CHF on engineered surfaces CHF on plain surfaces critical departure growth liquid quenching ring vapor wait						

reactor cladding materials [21–23], the literature on CHF enhancement in pressurized subcooled flow boiling, which is the heat transfer process used in most industrial applications, is rather small.

Many models have also been proposed to explain the mechanisms and predict the CHF enhancement in pool boiling, as shown by the schematic chart in Figure 1. Some of them are based on hydrodynamic instability [24-26]. Some models consider surface-wicking effects [5, 7, 10, 11, 13, 15, 27], thin-film evaporation [14], liquid trapping [18], or are based on a momentum balance at the liquid-vapor-solid triple contact line [9]. However, the applicability of these models is limited to specific surfaces. For instance, Chu et al. [9] developed a model to explain CHF enhancement based on the momentum balance at the solid-liquid-vapor contact line. While this model works well for their surfaces with cylindrical pillars, it does not seem to predict the CHF enhancements measured using square pillars of comparable dimensions by Dhillon et al. [11]. A similar conclusion can be reached if one tries to adopt the model developed by Dhillon et al. [11] to predict the results of Chu et al. [9].

In addition to all the deterministic models shown in Figure 1, a recent study [28] has revealed that the boiling crisis can be predicted using a stochastic bubble percolation model, and the associated CHF can be estimated using a heat flux partitioning model [29] describing how

energy is removed by the boiling process through several heat transfer mechanisms, e.g., microlayer evaporation, transient conduction (during the quenching phase), and forced convection. This percolation model requires several input parameters, namely bubble average growth time and frequency, nucleation site density, and average bubble footprint radius. Some of these parameters are difficult to estimate or even measure due to limitations in experimental imaging techniques (e.g., infrared thermometry), especially at high pressures, as bubbles become very small and have a very high nucleation frequency.

In this work, two special infrared heaters with nanoengineered super-hydrophilic coatings, i.e., a porous coating made of hydrophilic silica nanoparticles and a coating consisting of zinc oxide nanowires, were fabricated, and tested. Their boiling behavior in subcooled pressurized flow boiling conditions was studied using infrared thermometry. By running these experiments, the CHF enhancement using these super-hydrophilic coatings was compared to a plain "control" surface (i.e., a surface without any super-hydrophilic coating).

Also, the stochastic percolation model of the boiling crisis was re-casted by using bubble parameters which are less limited by the resolution of the infrared diagnostics. These parameters are the instantaneous bubble footprint radius distribution and instantaneous bubble density. The re-casted percolation model was validated

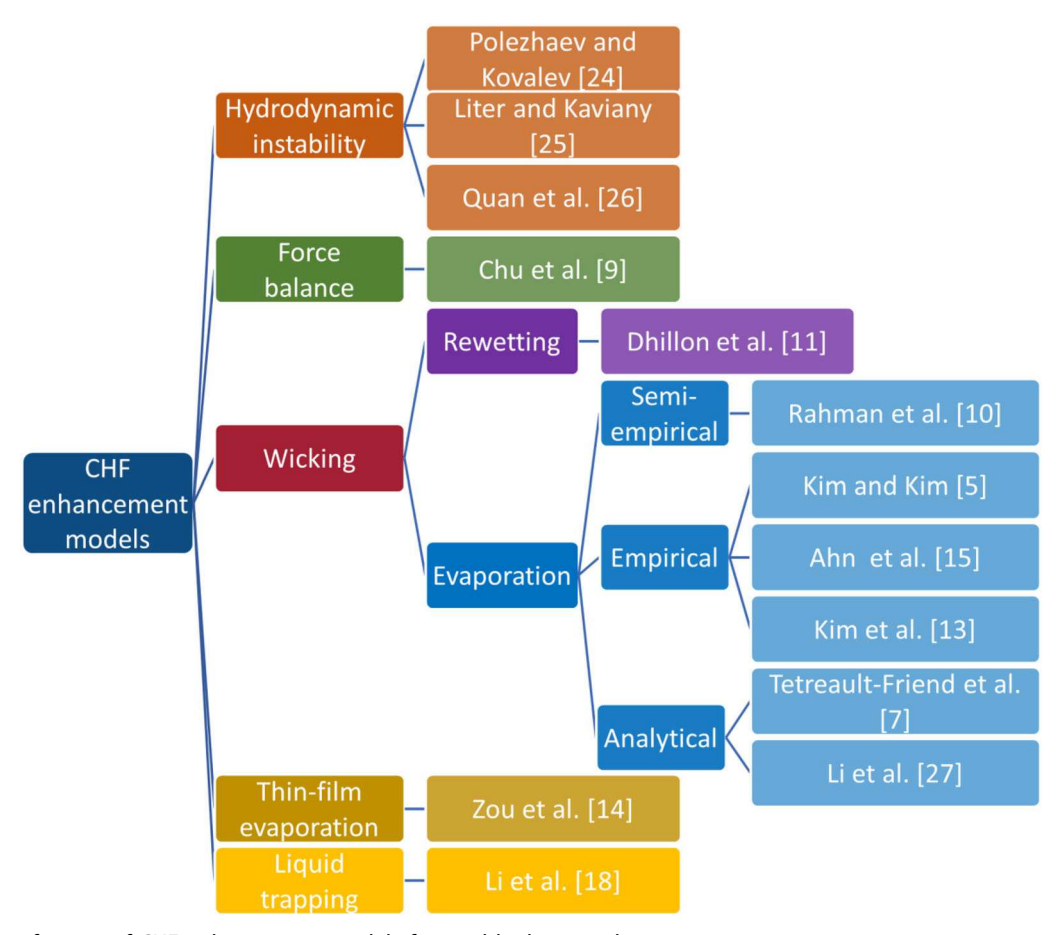


Figure 1. Classification of CHF enhancement models for pool boiling conditions.

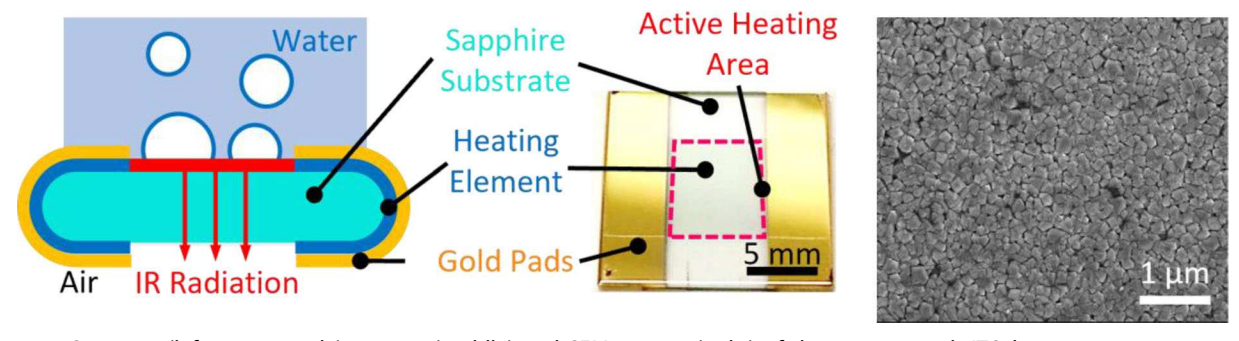


Figure 2. Structure (left, not to scale), picture (middle) and SEM images (right) of the nano-smooth ITO heater.

based on experimental data. The CHF enhancement observed on the super-hydrophilic surfaces was explained using a heat flux partitioning approach, according to the approach presented in Ref. [29].

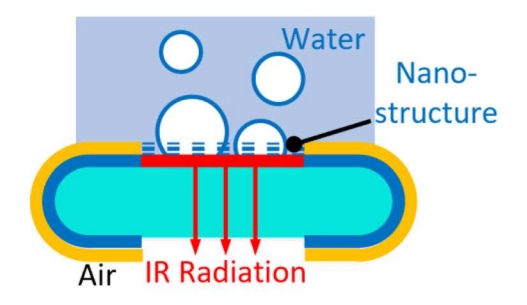
Infrared heaters

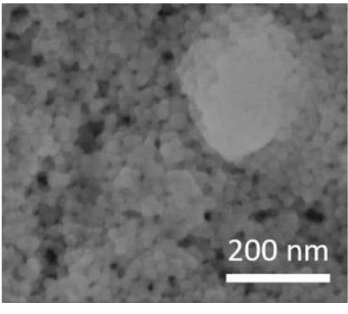
Nano-smooth heater

A nano-smooth heater is a heater with a nano-smooth, plain surface (i.e., a surface which is not coated with any kind of feature). Such heater has been used as "control" surface to benchmark the effect of various

super-hydrophilic porous features on the boiling process and the CHF limit. It consists of a sapphire substrate coated with an indium tin oxide (ITO) layer, as sketched in Figure 2. A detailed description of this heater design can be found in Ref. [29].

The roughness of this plain, ITO-sapphire heater is approximately 10 nm [29]. It is determined by rare imperfections on the underlying sapphire substrate and grains of the ITO film, as revealed by the scanning electron microscope (SEM) image shown in Figure 2. Its static contact angle measured with the sessile droplet technique was $86.5^{\circ} \pm 3^{\circ}$ in ambient air at room temperature [29].





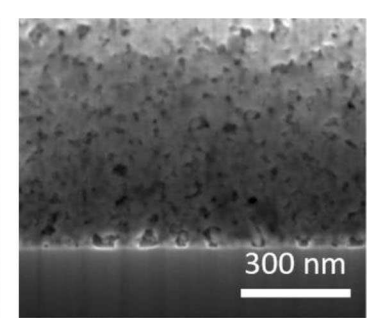
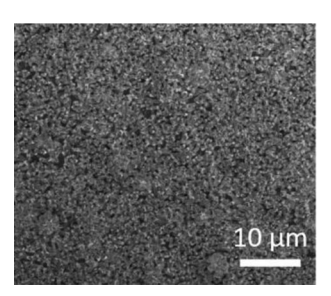


Figure 3. Sketch of the nano-porous heater (left, not to scale), top view (middle) and cross-section view (right) SEM images of the nano-porous layer.



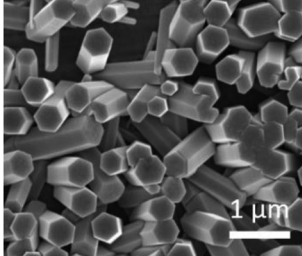


Figure 4. SEM images of the nanowires surface.

Nano-porous heater

The nano-porous heater was obtained by coating the plain ITO-sapphire heater with hydrophilic silica nanoparticles, as shown in Figure 3. Precisely, silica nanoparticles were coated on top of the surface in contact with water (including the active heating area) using a layer-by-layer deposition technique [30]. Based on the study carried out by Tetreault-Friend et al. [7], the porous layer was fabricated to be 1.8 µm thick to maximize CHF enhancement. The diameter of the silica nanoparticles was 20 nm. The diameter of the pores formed by the nanoparticles deposition was in the same order of magnitude. Figure 3 also shows SEM images of the porous layer.

The nano-porous layer exhibited a super hydrophilic behavior (as its static contact angle was approximately 0°) due to the intrinsic porosity and hydrophilicity of the silica particles that create capillary force within the nanoscale pores. The wicking number of this surface was 0.88 ± 0.27 , measured according to the procedure proposed in [10].

Nanowire heater

The third heater features a boiling surface covered by zinc oxide nanowires. It has the same configuration as the nano-porous heater shown in Figure 3. However, the heating layer of this heater was made of titanium (instead of ITO) and it was 500 nm thick. Titanium was used because it has a better bonding with the zinc oxide

nanowires compared to ITO. Otherwise, this heater had the same active heating area as the nano-smooth and nano-porous heaters. The zinc oxide nanowires were created on top of the active heating area using a fabrication procedure similar to the one presented in [31]. The average diameter of the nanowires was approximately 200 nm, and the average height was approximately 2 $\mu m.$ Figure 4 shows the SEM images of the nanowires.

The nanowire surface also exhibited superhydrophilicity due to the capillary force in the microscale gaps formed by the nanowires. The measured wicking number of this surface was 0.41 ± 0.15 .

Experimental setup and procedures

In this study, subcooled flow boiling experiments at 1 bar and 4 bars were conducted in the flow loop sketched in Figure 5(B). More details about the test facility can be found in Ref. [32]. Briefly, the test section holding the heaters is shown in Figure 5(A). The flow channel had a rectangular $3 \, \text{cm} \times 1 \, \text{cm}$ cross section. The IR heaters were installed in a ceramic cartridge made of Shapal TM. In order to achieve fully developed upward flow conditions in the test section, an entrance region with the same flow channel dimensions and a length of about 60 hydrodynamic diameters foreruns the test section.

An IR camera was used to monitor the temperature of the boiling surface when the experiments were conducted. When the boiling crisis occurred, the radiation emitted by the surface spiked, indicating a rapid increase of the surface temperature. When this radiation spike was observed, the power was shut down to avoid damaging the heater. After the test, the infrared videos collected by the camera were postprocessed to obtain time-dependent temperature and heat flux distributions on the boiling surface and verify that indeed the radiation spike coincided with spreading of a large dry patch with poor heat transfer properties (with heat flux close to zero) on the boiling surface.

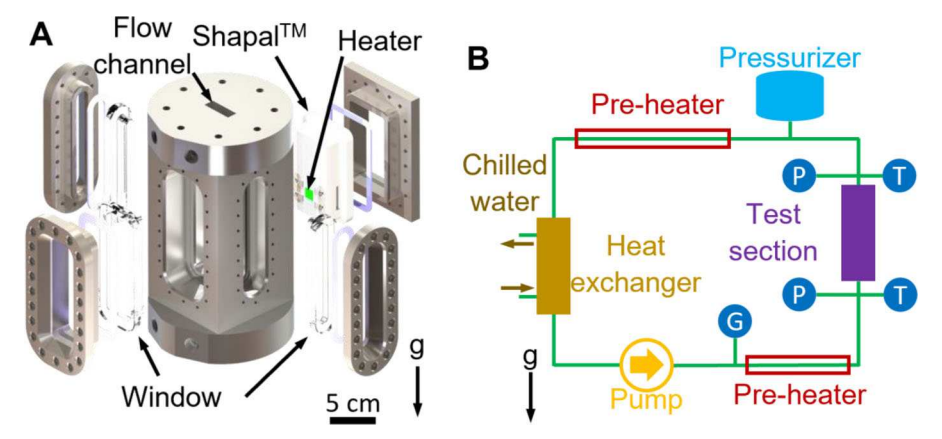


Figure 5. Test section (A) of the experiments is installed in the experimental loop (B). In (B), "P" represents the pressure sensor, "T" represents the temperature sensor, and 'G' represents the flow meter.

In each boiling test, the mass flux and subcooling were set at 1000 kg/(m²·s) and 10 K, respectively. This specific set of operating conditions was used for all the tests to separate the effects created by the surface conditions from all other effects. To control the imposed heat flux, the voltage applied across the active heater area was increased in steps until the boiling crisis occurred. The increments of the heat flux were approximately 0.3 MW/m² at the beginning of the boiling process. They were reduced to approximately 0.1 MW/m² near the CHF. The voltage and current were recorded with a frequency of 10 kHz using a high-speed data acquisition system. Based on the current and voltage measurements, the average heat flux on the boiling surface was evaluated as:

$$q_{CHF,e}^{"} = \frac{U \times I}{A_{heat}}$$
 (1)

where U is the measured voltage, I is the measured current, and A_{heat} is area of the active heating surface. The uncertainty of the heat flux is around ±3%, and it is mainly caused by the measurement of the active heating area.

The temperature distribution of the boiling surface was measured using IR thermometry. First, IR radiation was collected by a high-speed IR camera (IRC 806S) at a frame rate of 2500 FPS (frame per second) and with a pixel resolution of 116 µm. Then, the recorded IR radiation was converted to temperature distribution according to calibration technique proposed in [33], consisting of an inverse problem (solved iteratively) coupling conduction heat transfer in the substrate and optical radiation. The distribution of heat flux to water is also a result of the three-dimensional conduction model used for the calibration process [33]. The accuracy and precision of the temperature measurements are smaller than 1.1 °C and 0.1 °C, respectively.

An example of the instantaneous temperature and heat flux distributions on the surfaces at 1 and 4 bars are shown in Figures 6 and 7, respectively. For illustration purposes, the distributions shown in these figures are cropped to a size of approximately $7 \,\mathrm{mm} \times 7 \,\mathrm{mm}$. The space resolution that could be achieved as a compromise between temporal resolution and heater area (to image the largest possible boiling area with the shortest possible time step) corresponds to a pixel resolution of 116 µm/pixel. The uncertainty resulting from pixel size is, however, small compared to the standard deviation of the parameters that was measured by postprocessing these images, which is mostly determined by the statistical variation of the latter. Readers interested in the aspects related to uncertainty quantifications are directed to Ref. [32] for more details.

The ring-shaped regions in the heat flux distributions shown in Figure 6 for the 1 bar tests denote the evaporation of the liquid microlayer that forms when bubbles grow over the boiling surface. Due to the large amount of heat removed by microlayer evaporation, the temperature of the boiling surface where microlayer is evaporating decreases rapidly, as shown by the temperature distributions in Figure 6. When the entire microlayer has evaporated, dry patches form on the surface. These patches are called "dry" to indicate that the surface is in contact with vapor. They can be recognized because, due to the poor cooling properties of vapor, the local heat flux is very small (practically zero). They correspond to the dark blue regions in the heat flux distributions in Figure 6. As the heat transfer from the surface to the bulk liquid is poor, the temperature within these dry patches increases rapidly. Indeed, as shown by the temperature distributions, the temperature in these dry spots is higher than in their surroundings.

In the high-pressure tests, i.e., at 4 bars, bubbles become much smaller, as indicated by the smaller high

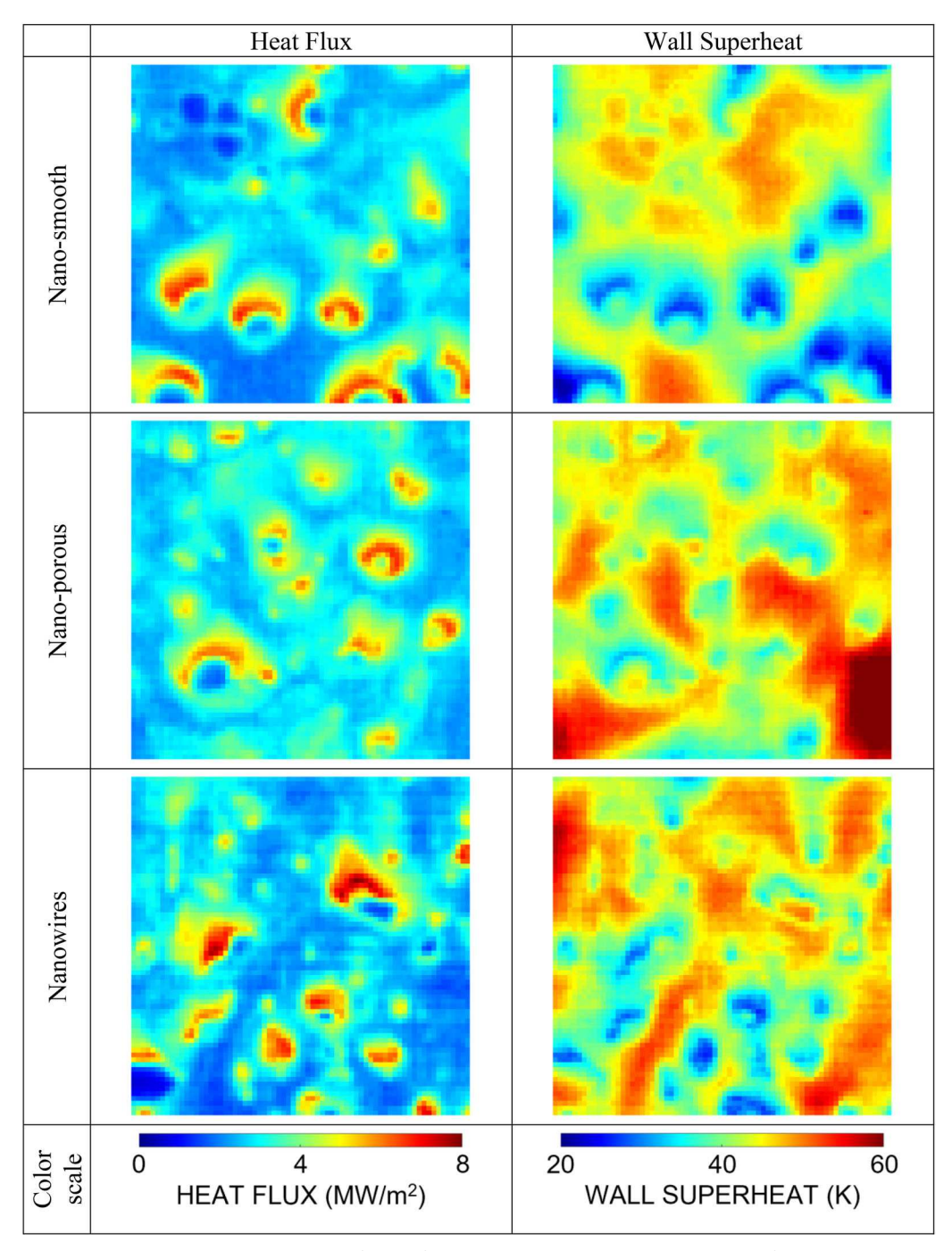


Figure 6. Sample wall superheat (right) and heat flux (left) distribution on nanoengineered surfaces at 1 bar. The average heat flux of all the distributions is around 3 MW/m². The size of all distributions is cropped to be around 7 mm by 7 mm.

heat flux dots shown in the heat flux distributions of Figure 7. It is practically impossible to detect dry patches, if any. Importantly, in these high-pressure tests, due to the limitations in the spatial and temporal resolutions of the IR camera, it is more much difficult (if not impossible) to extract the bubble parameters, e.g., growth time and departure frequency, using the infrared measurements. It is however possible to measure the instantaneous bubble density and their size distribution.

Results and discussions

Boiling curves and CHF enhancement

Figure 8 shows the boiling curves for two nano-engineered surfaces at 1 and 4 bars. The boiling curve of the nano-smooth ITO surface is also plotted. The CHF values for the nano-smooth, nano-porous, and nanowire surfaces are $3.86\,\mathrm{MW/m^2}$, $4.46\,\mathrm{MW/m^2}$, $4.47\,\mathrm{MW/m^2}$ for 1 bar and $4.65\,\mathrm{MW/m^2}$, $5.84\,\mathrm{MW/m^2}$, $5.42\,\mathrm{MW/m^2}$ for 4 bars, respectively. The CHF values are summarized

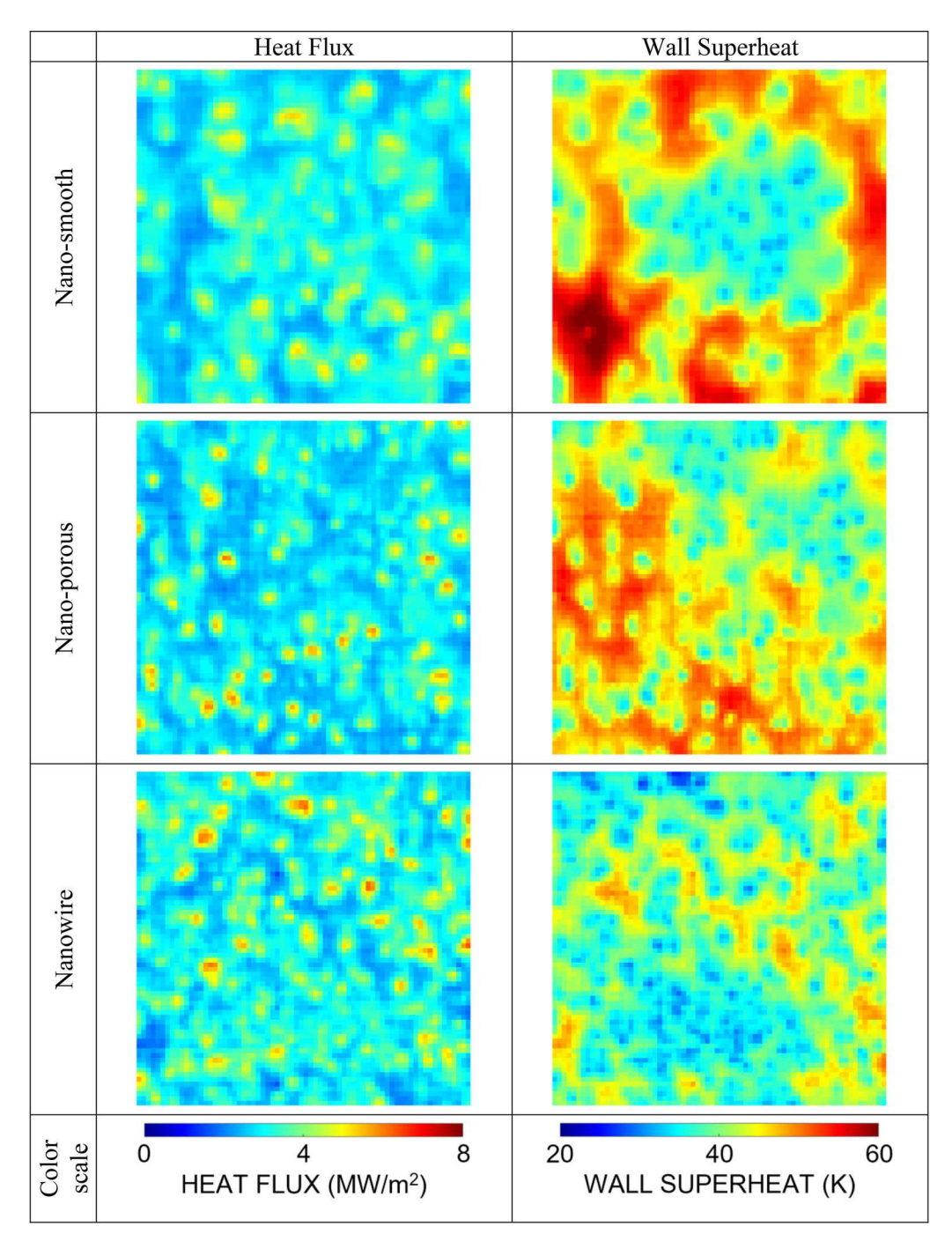


Figure 7. Sample wall superheat (right) and heat flux (left) distribution on nanoengineered surfaces at 4 bars. The average heat flux of all the distributions is around 3 MW/m². The size of all distributions is cropped to be around 7 mm by 7 mm.

in Table 1. At 1 bar, both the nano-porous surface and the nanowire surface increase the CHF by roughly 15% (0.6 MW/m²) compared to the nano-smooth surface. Interestingly, the enhancement is higher at 4 bars. Precisely, the CHF enhancement is 25% (1.2 MW/m²) for the nano-porous layer and 17% (0.8 MW/m²) for the nanowire surface. The nano-smooth surface, nano-porous layer and nanowire surface had also been tested in pool boiling by our group in an earlier work [34]. The pool boiling CHF values were 1.17, 2.21, and 1.46 MW/m², respectively. The pool boiling CHF enhancement was 89% (1.04 MW/m²) for the nano-porous surface and 25% (0.29 MW/m²) for the nanowire surface.

The CHF enhancements from the two nanoengineered surfaces in pool boiling are not far from values that can be predicted using wicking number by the semi-empirical method proposed in Ref. [10], i.e.,

$$q_{\text{CHF, e}}^{\prime\prime}=q_{\text{CHF, p}}^{\prime\prime}(1+Wi) \tag{2}$$

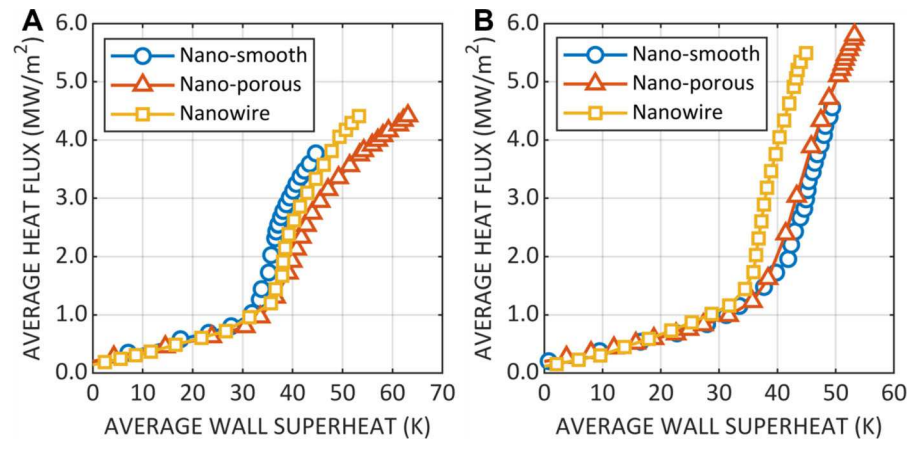


Figure 8. Boiling curves for different surfaces at 1 bar (A) and 4 bars (B).

Table 1. Summary of bubble parameters, filling factors, and CHF values.

	,	1 '	<i>J</i> ,			
Pressure	Surface	$\langle R \rangle$ (mm)	$ ho_b$ (1/cm ²)	Experiment η_c	Simulation η_c	CHF (MW/m ²)
1 bar	Nano-porous	0.37	96 ± 8	0.41 ± 0.03	0.55 ± 0.01	4.46 ± 0.06
	Nanowire	0.36	98 ± 10	0.40 ± 0.04		4.47 ± 0.04
	Nano-smooth	0.46	60 ± 8	0.39 ± 0.05		3.86 ± 0.09
4 bars	Nano-porous	0.21	377 ± 20	0.53 ± 0.03	0.64 ± 0.01	5.84 ± 0.04
	Nanowire	0.19	424 ± 19	0.49 ± 0.02		5.42 ± 0.07
	Nano-smooth	0.28	212 ± 11	0.53 ± 0.03		4.65 ± 0.09

where $q''_{CHF,e}$ is the CHF on the engineered surfaces, $q''_{CHF,p}$ is the CHF on the plain surfaces and Wi is the wicking number:

$$Wi = \frac{V_0'' \rho_l}{\rho_v^{1/2} [\sigma g(\rho_l - \rho_v)]^{1/4}}$$
 (3)

where ρ_l is the liquid density in saturation conditions, ρ_v is the vapor density in saturation conditions, σ is the surface tension, g is the gravity constant, and V_0'' is the initial volumetric flux (in m/s) of the wicking flow measured with the wicking test proposed in Ref. [10].

This method, however, seems to largely overestimate the CHF enhancements in flow boiling. Since the wicking number proposed in Ref. [10] only depends on physical properties of the working fluid, it would predict the same relative CHF enhancement in pool boiling and flow boiling. However, our experimental data show a much lower relative enhancement in flow boiling than in pool boiling. Besides, this semi-empirical approach also seems to contradict our experimental data at 4 bars. Since the wicking flow is driven by the capillary pressure which is proportional to surface tension (σ) and slowed down by the flow resistance which is proportional to fluid viscosity (μ), V_0'' in Eq. (3) should scale as σ/μ (whose units are also m/s). Thus, Eq. (3) can be rewritten as:

Wi
$$\propto \frac{(\sigma/\mu)\rho_{\rm l}}{\rho_{\rm v}^{1/2}[\sigma g(\rho_{\rm l}-\rho_{\rm v})]^{1/4}}$$
 (4)

With water properties at saturation, Eq. (4) suggests that the wicking number decreases with pressure, as shown in Figure 9(A). Correspondingly, the semi-empirical approach proposed in Ref. [10] would predict a decreasing CHF enhancement as the pressure increases. However, our experimental data show that both the absolute and the relative CHF enhancements at 4 bars are higher than at 1 bar. Interestingly, if only σ/μ is plotted, as shown in Figure 9(B), it can be shown that this term increases between 1 and 4 bars. In fact, it peaks around 10 bars. This indicates that while the wicking flow increases between 1 and 4 bars, the wicking number decreases.

The discrepancies between the model proposed in Ref. [10] and our experimental data suggest that wicking property of the surface may not be the only reason for CHF enhancement. Other factors, such as bubble dynamics, may have more significant effects on CHF enhancement, especially in flow boiling. In passing, it is noted that the wicking number proposed by Rahman et al. [10] assumes that the characteristic length scale of the process is the Laplace length. However, the presence of the flow and surface may change this characteristic length. In the future, attempts could be made to redefine the wicking number based on the bubble size, describing how the later changes due to the presence of the flow.

Boiling crisis prediction with revised percolation Monte Carlo model

In a recent work from our group, the boiling crisis has been found to be closely related to a critical state in the bubble interaction phenomenon, described as percolation

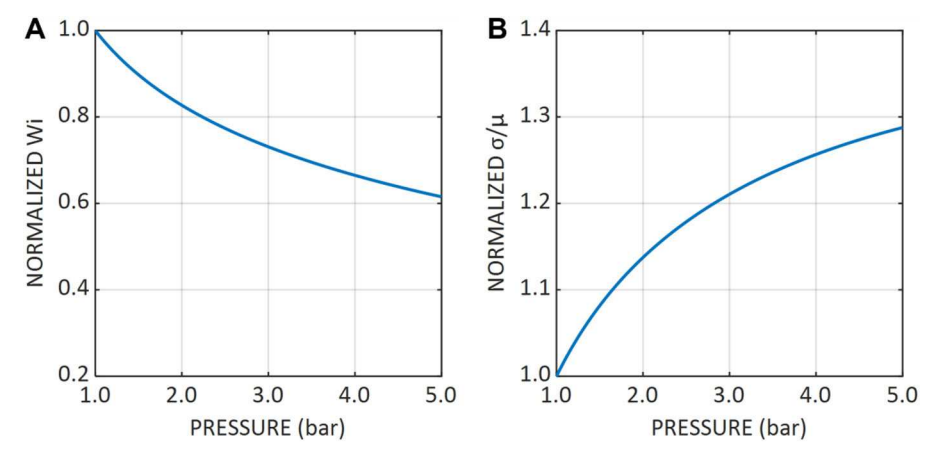


Figure 9. Normalized wicking number (Wi) with pressure (A) and normalized σ/μ with pressure (B). The normalized value is calculated by dividing values at different pressures with the value at 1 bar.

process [28]. This critical state can be quantified using nucleation site density, product of bubble growth time and departure frequency, and average bubble footprint radius.

However, in high pressure conditions, it is difficult to measure bubble growth time due to limitation in the acquisition rate of the infrared camera. For instance, the temporal resolution of the infrared camera used in this work is 0.4 ms (corresponding to 2500 frames per second), which is very close to the bubble growth time, especially for the 4 bars tests. Therefore, the bubble growth time at 4 bars extracted by postprocessing the IR recordings would have large uncertainties, which prevents the application of the percolation model to the high-pressure tests.

To overcome this difficulty, the Monte Carlo (MC) percolation model was re-casted by using the instantaneous bubble density and instantaneous bubble footprint radius. The instantaneous bubble density is the density of bubbles on the heater at any given moment. The instantaneous bubble footprint radius is the radius of all the bubbles at the bubble base (i.e., on the boiling surface) at a given moment (i.e., it is not the bubble departure radius). In high pressure conditions, the instantaneous density and the instantaneous footprint radius can be obtained with higher accuracy compared to the boiling parameters required by the stochastic bubble percolation model (i.e., nucleation site density, growth time, departure frequency, and average footprint radius). Postprocessed IR recording where the bubbles are represented by circles of equivalent footprint area are shown in Figure 10. A detailed description of the postprocessing required to identify the bubbles can be found in a previous paper from our group [32]. To clarify, the white solid line circles in Figure 10 are not microlayer footprints. They represented circles with the same area as the associate bubble footprints. The undetected "hot spots" shown

in Figure 10 disappears shortly after the frame shown in Figure 10 without developing into larger patches. They are too small to have significant effects on the boiling process. Importantly, the uncertainty caused by ignoring these tiny bubbles does not affect the size distribution of bubbles, which accounts for the time and statistical variability of bubbles on the boiling surface throughout the period of acquisition of the IR images, i.e., 2 s per heat flux. This duration is sufficient to achieve statistically converged distributions.

By counting the bubble number, the instantaneous bubble density can be easily calculated. At the boiling crisis, 50-100 frames were analyzed to count the bubbles on each frame and average them to get this parameter. The average value was also verified to be statistically converged. This procedure was repeated multiple times for the same surface and operating conditions and the difference was ascertained to be smaller than the standard deviation shown in Table 1. The instantaneous bubble footprint radius distribution was then evaluated by collecting the radii of all the bubbles on many frames. The distributions (probability density function – PDF) of the normalized bubble footprint radius $(R/\langle R \rangle)$ are shown in Figure 11. The distributions on each surface were normalized by the average radius for comparison. It can be found that the normalized distributions for different surfaces at the same pressure can be well-fitted using a gamma distribution. However, different pressures would result in different shapes for the gamma distributions.

Nominal values of the measured instantaneous bubble density and average footprint radius with their standard deviations are summarized in Table 1. These standard deviations are determined by the statistical variation of the quantities. Measurement errors for these quantities are negligible compared to their statistical fluctuations and do not have significant effects

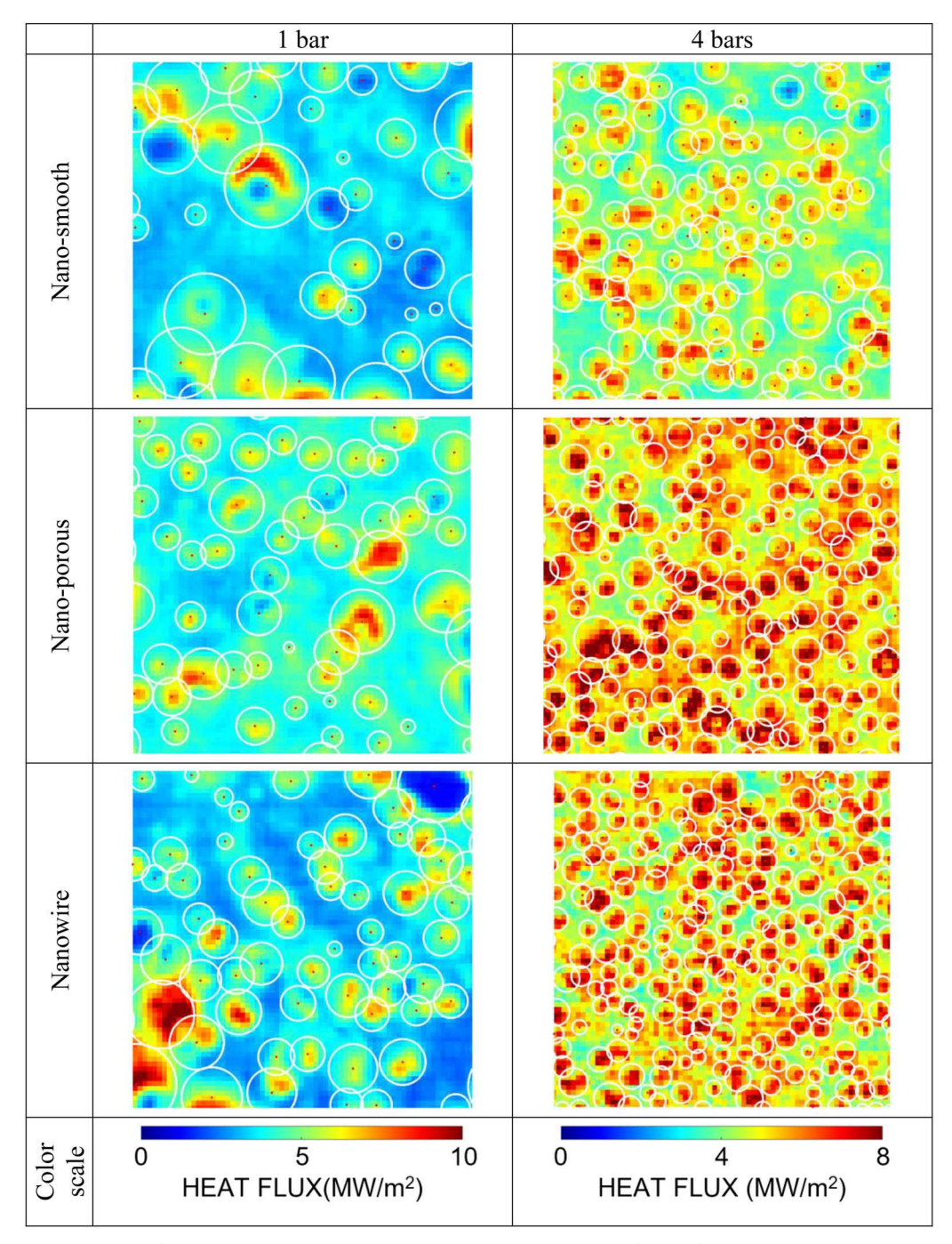


Figure 10. Detected bubble footprint (white circles) at the boiling crisis on top of heat flux distributions. The size of all distributions is cropped to be around 7 mm by 7 mm.

on their statistical distributions. Readers interested in the aspects related to uncertainty quantifications are directed to Ref. [32] for more details.

The percolation model of the boiling crisis described in Refs. [28, 29, 35] assumes that the crisis is triggered by an instability in the bubble interaction process, which can be captured by a stochastic model. Briefly, a number of nucleation sites is randomly generated on a virtual boiling surface (according to the measured nucleation site density, N"). Then, each site is re-visited

to generate a bubble with a probability prescribed by the measured product of the bubble frequency, f, and the bubble growth time, f Finally, the bubble radius is chosen according to the measured radius distribution (typically a gamma function or exponentially damped function). As the number, size, and probability (i.e., growth time \times frequency) of bubbles increase, they tend to form large vapor patches. There is a critical combination of these parameters for which these patches merge together and form a stable vapor layer. It

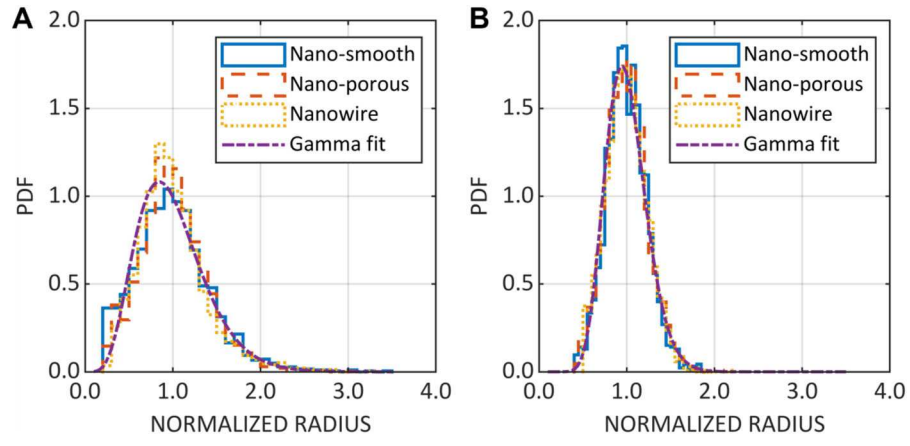


Figure 11. Distribution of the normalized instantaneous bubble footprint radius at 1 bar (A) and 4 bars (B).

was found in Ref. [35] that this critical combination is described by a simple non-dimensional law:

$$N''\pi \langle R \rangle^2 ft_g \sim 1 \tag{5}$$

where < R> denotes the average bubble footprint radius.

In the re-casted version of the percolation model, bubbles are generated at random locations one after another until the total number of the bubbles reaches the limit set by the instantaneous bubble density, $\rho_{\rm b}$. The radius is chosen according to the experimentally measured bubble footprint radius distribution. According to the percolation theory [28, 35], the revised model predicts criticality when

$$\rho_{\rm b}\pi\langle R \rangle^2 = \eta_{\rm c} \tag{6}$$

where η_c is the critical filling factor. According to fundamental continuum percolation studies [36], the critical filling factor is only a function of the shape of the radius distribution. The ratio between the characteristic size of the active heating area and the average footprint radius may also affect the critical filling factor [37]. This effect is negligible in this work as the active heating area and the average footprint radius for different surfaces are similar. However, as the shape of distribution at 1 and 4 bars are different, two critical filling factors for 1 and 4 bars should be expected.

To determine the value of η_c with the footprint radius distribution measured from our experiments, MC simulations were carried out following the procedure described here. A surface was firstly set with the same size of the active heating area of the surfaces. Then, a certain number of bubble footprints were generated with a radius sampled from the gamma distributions fitted from our experimental data shown in Figure 11. Finally, the bubble footprints were randomly distributed over the surface. If a nucleation site was covered by a bubble, it could not generate bubbles. A qualitative comparison of footprints between our simulation and experiments are shown in Figure 12.

Once the bubble footprint distributions were collected, the size of the largest bubble cluster and the second largest bubble cluster, i.e., G (giant cluster) and SG (second giant cluster), were recorded. Then the simulation process was repeated until a converged distribution of G and SG was obtained. The bivariate histograms of G and SG collected in our simulations are plotted in Figure 13. According to our earlier studies [28, 29, 35], G is slightly larger than SG when the system is subcritical, as shown in Figure 13(A) where the peak of the G-SG bivariate histogram is near the line representing G = SG. Then the number of bubbles in the simulation was increased and the process was repeated until a supercritical state where G is much larger than SG was found, as shown in Figure 13(B), where the peak in the G-SG bivariate histogram has shifted toward lower right corner. Finally, the critical point was identified by refining the number of bubbles in our simulation between the subcritical and supercritical states. For the bubble radius distribution measured at 1 bar, it was found that the critical filling factor is 0.55 ± 0.01 . For the bubble radius distribution measured at 4 bars, the critical filling factor was found to be 0.64 ± 0.01 .

Simulations using gamma distributions with different average footprint radius were also carried out. In these simulations, the average footprint radius of these distributions was changed as a function of heat flux and surface according to our measurements summarized in Table 1. Based on the results, it was found that the critical filling factor does not depend on the average footprint radius as long as the distribution of the normalized radius is the same, which agrees with previous fundamental continuum percolation studies [36].

Then, the critical filling factor identified in our simulation was verified with our experimental data.

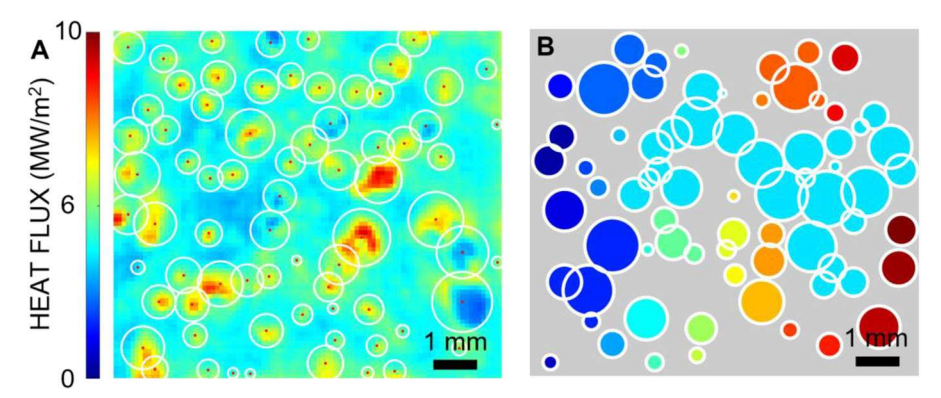
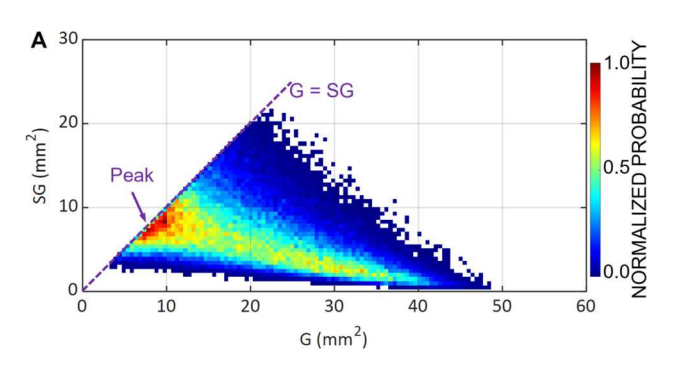


Figure 12. Comparison of bubble footprints measured experimentally (A) and obtained by the Monte Carlo simulations (B). The different colors in (B) represent different bubble clusters (i.e., groups of merged bubbles).



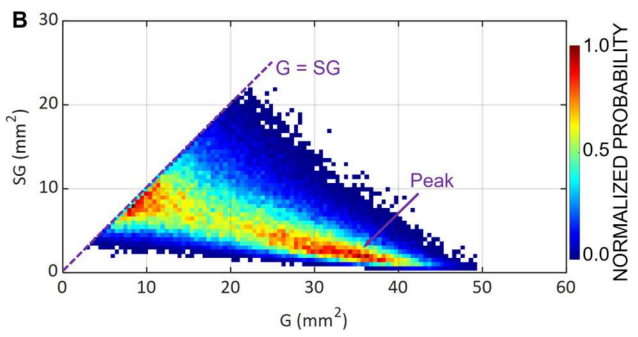


Figure 13. Bivariate histograms of the area of the largest cluster (G) and second largest cluster (SG) at a subcritical (A) and supercritical (B) state. The radius distribution in these simulations is the gamma distribution fitted from experiments at 1 bar. The instantaneous bubble density is $125 \, \mathrm{cm}^{-2}$ for (A) and $130 \, \mathrm{cm}^{-2}$ for (B). The corresponding filling factor is 0.54 for (A) and 0.56 for (B).

Since the boiling crisis is the critical state of the bubble interaction, the filling factor was calculated using the instantaneous bubble density and the average footprint radius extracted from the boiling crisis step for each surface. The results are summarized in Table 1. From Table 1, it can be seen that the experimental filling factors for different surfaces agree well with each other at a given pressure and as predicted by the model, increase with pressure for each surface. However, there is a small difference between the experimental filling factor and the simulation filling factor. This discrepancy may be due to a limit in the pixel resolution of the

optical setup. Bubbles smaller than 110 μ m cannot be detected by the current IR diagnostics, which may lead to an underestimation of the experimental instantaneous bubble density. Nevertheless, the experimental results are aligned with the predictions of the re-cast percolation model, i.e., Eq. (6), and corroborate the idea that the boiling crisis can be viewed as a percolation phase transition triggered by an instability in the bubble interaction process.

Heat flux partition

According to wall heat flux partitioning models (e.g., see [29]), the heat flux removed during nucleate boiling can be decomposed in several mechanisms, involving both single phase (i.e., without phase-change) and two-phase (i.e., with phase change) heat transfer. Single-phase heat transfer mechanisms involved in the boiling process include transient conduction (during quenching) and forced convection. Two-phase heat transfer occurs "at the wall" by evaporation of liquid in the microlayer and at the liquid-vapor-solid triple contact line. By postprocessing the heat flux distributions obtained using the IR thermometry technique, the contribution of evaporation and non-evaporation heat transfer mechanisms for the three surfaces at the boiling crisis are quantified, as shown in Figure 14.

From Figure 14, it can be seen that CHF enhancement is enabled by an increase of both the evaporation and single-phase heat transfer modes. The evaporation heat transfer mainly occurs due to the evaporation of microlayers. To mimic the ring-shaped microlayer evaporation shown in Figure 10, the area covered by the microlayer in a unit area can be expressed using:

$$a_{\text{micro}} = \rho_{\text{b}} 2\pi \langle R \rangle W_{\text{r}} \tag{7}$$

where W_r is the width of the microlayer ring. At the boiling crisis (i.e., for the CHF), Eq. (7) can be rewritten by combining it with Eq. (6):

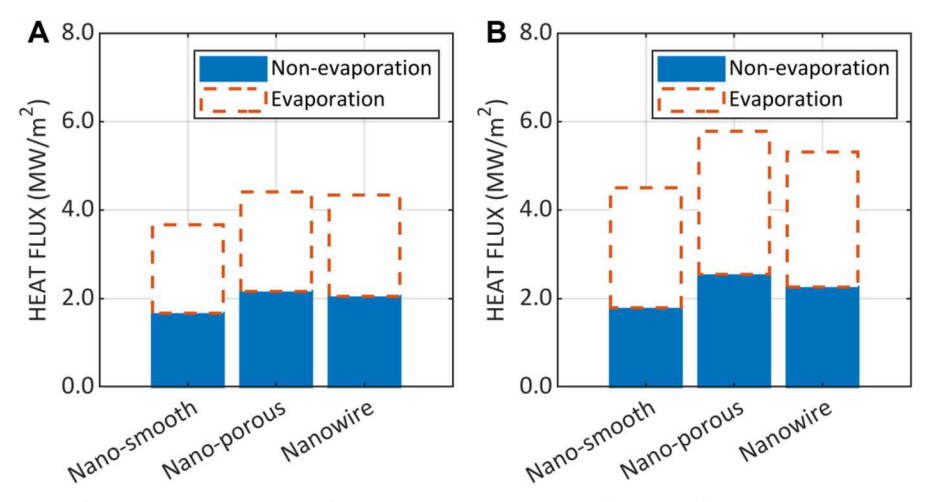


Figure 14. Measured heat flux partitioning right before the boiling crisis on different surfaces at 1 bar (A) and 4 bars (B).

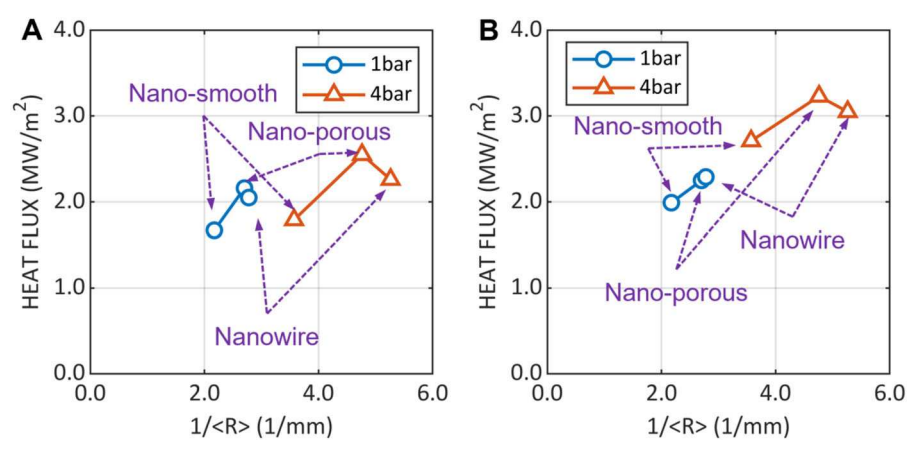


Figure 15. Non-evaporation heat flux vs. inverse of the average instantaneous bubble footprint radius (A), Evaporation heat flux vs. inverse of the average instantaneous bubble footprint radius (B).

$$a_{\text{micro}} = \frac{\eta_c W_r}{\langle R \rangle} \tag{8}$$

where η_c is, as shown, a constant at the boiling crisis. In a first-order approximation, the width of the microlayer ring can be assumed constant, and the microlayer area and the evaporation heat flux at the boiling crisis become inversely proportional to the average instantaneous bubble footprint radius. This argument is supported by our experimental data shown in Figure 15, where the evaporation heat flux is plotted vs. 1/<R > for different surfaces. Although only three surfaces were tested, the results show that the evaporation heat flux increases as the bubble footprint radius decreases (and the number of bubbles increase).

The non-evaporation heat flux is more complex since it consists of both quenching heat flux and forced convection heat flux and it is difficult to decouple them. However, according to the analysis in [29], it may be assumed that single-phase heat flux at the CHF only consists of quenching heat flux (i.e., it may be assumed that forced convection effects are practically negligible), and it can be simplified into:

$$q_{\text{quench}}'' \propto K \rho_{\text{dep}} f \pi r_{\text{dep}}^2 t_{\text{w}} h_{\text{q}} (T_{\text{wall}} - T_{\text{b}}) \tag{9}$$

where K is the influence area factor, $\rho_{\rm dep}$ is the density of departure bubbles, tw is the bubble wait time, f is the bubble frequency, r_{dep} is the bubble departure radius, h_q is the transient conduction coefficient, Twall is the wall temperature, and T_b is the bulk liquid temperature. The bubble frequency f can be written as $1/(t_g + t_w)$, where t_g is the bubble growth time. Since at the boiling crisis the bubble wait time is in the same order as the bubble growth time according to our experimental data [34], f can be approximated as 0.5/t_w. The transient conduction heat transfer coefficient during this transient conduction phase can be calculated as $h_q = \epsilon_l (\pi/t_q)^{0.5}$, where ϵ_l is the thermal effusivity of the liquid and t_q is the time elapsed since the rewetting of the surface. Then, Eq. (9) can be rewritten as:

$$q_{quench}^{\prime\prime} \propto 0.5 K \rho_{dep} \pi r_{dep}^2 \epsilon_l \sqrt{\frac{\pi}{t_a}} (T_{wall} - T_b) \eqno(10)$$

where $ho_{
m dep}\pi r_{
m dep}^2$ represents the properties of departure bubbles that can be considered as proportional to the bubble footprint properties shown by Eq. (6). As discussed, Eq. (6) is constant at the boiling crisis. Therefore, the dependence of the quenching heat flux on the term $\rho_{\rm dep}\pi r_{\rm dep}^2$ disappears at the boiling crisis. So, quenching heat flux at the boiling crisis becomes only a function of the time elapsed in the quenching phase (i.e., the wait time) and the wall superheat. Specifically, a shorter wait time means a higher quenching heat flux at a given surface temperature.

On nanoengineered surfaces, bubble size is usually smaller as shown by the average footprint radius in Table 1. A smaller bubble size typically leads to a faster bubble life cycle. Consequently, the wait time in a faster bubble life cycle is shorter, which eventually results in a higher quenching heat flux. In other words, the quenching heat flux on nanoengineered surfaces is also likely to be proportional to the inverse of the instantaneous bubble radius. This conclusion is also supported by our experimental data shown in Figure 15 where the quenching heat flux increases as the footprint radius decreases from nano-smooth surfaces to nano-engineered surfaces.

In summary, the enhancement of the CHF on nanoengineered surface comes from not only the increase of the evaporation heat flux, as assumed by many of the pool boiling models captured in Figure 1 [5, 7, 13, 15, 27], but also the increase of the quenching heat flux. The enhancement of evaporation heat flux occurs due to an increase in total microlayer area by smaller and denser bubbles. Instead, the enhancement of quenching heat flux can be attributed to the higher transient heat conduction coefficient generated by faster bubble life cycles.

Conclusions

In this work, it was shown that the CHF in subcooled flow boiling at high pressures can be enhanced by surfaces coated with a super-hydrophilic silica nano-porous layer and super-hydrophilic zinc oxide nanowires. The CHF enhancement was around 15% for both coatings at 1 bar. At 4 bars, the CHF enhancement was around 17% for the nanowire surface, and around 25% for the nanoporous surface.

Time-dependent temperature and heat flux distributions and bubble dynamics at the boiling surface were captured using infrared thermometry and specially designed IR heaters. The temperature and heat flux distributions were used to extract key parameters of the boiling process including instantaneous bubble density and instantaneous bubble footprint radius.

The difficulty of applying the original percolation model proposed in Ref. [28, 35] was overcome by developing a revised percolation model based on instantaneous bubble density and bubble footprint radius distribution. The revised model has been validated with our experimental data in flow boiling at 1 and 4 bars, and with different surfaces. It was proved that the nondimensional term $\rho_b \pi \langle R \rangle^2$ can be used as a parameter to predict the boiling crisis on nanoengineered surfaces in subcooled flow boiling, especially at high pressures where the bubble growth times become difficult to measure. The success of the revised model also corroborated the hypothesis that the boiling crisis is a percolative phase transition triggered by an instability in the bubble interaction process.

Also, the experimental CHF enhancement was analyzed by partitioning it into non-evaporation heat flux and evaporation heat flux. Our results suggest that nanoengineered surfaces may enhance CHF by modifying the bubble dynamics to achieve a larger instantaneous bubble density, a smaller instantaneous bubble footprint radius and a faster bubble cycle. The larger instantaneous bubble density and the smaller instantaneous bubble footprint radius resulted in a higher microlayer coverage which led to a higher evaporation heat flux. The shorter bubble cycle led to a higher non-evaporation quenching heat flux. Together, they made the CHF on the nanoengineered surfaces higher than the nano-smooth reference surface.

Acknowledgments

The results presented in this article were obtained in research projects sponsored by the National Science Foundations and the Exelon Corporation through its membership in the MIT Energy Initiative.

Disclosure statement

No potential conflict of interest was reported by the authors.

Notes on contributors



Chi Wang is a Ph.D. student in the Department of Nuclear Science Engineering, Massachusetts Institute Technology, Cambridge, Massachusetts, USA. He received his M.Sc. degree from School of Nuclear Science and Engineering, Shanghai Jiao Tong University, Shanghai, China. He is investigating the mechanisms of

critical heat flux enhancements on engineered surfaces with infrared thermometry.





Guanyu Su is a Postdoctoral Associate in the Department of Nuclear Science and Engineering, Massachusetts Institute of Technology (MIT), Cambridge, Massachusetts, USA. He received his Ph.D. in Nuclear Science and Engineering from MIT in 2018. His research interests include boiling heat transfer, two-phase flow and molten salt.



Olorunsola Akinsulire is a M.Sc. student in the Department of Nuclear Science and Engineering, Massachusetts Institute of Technology (MIT), Cambridge, Massachusetts, USA. He received his B.S. degree from MIT. He has been working on the fabrication and characterization of engineered surfaces, especially the nanowires

made of zinc oxide.



Limiao Zhang is a Ph.D. student in the Department of Nuclear Science and Engineering, Massachusetts Institute of Technology, Cambridge, Massachusetts, USA. She received her M.Sc. degree from the School of Reliability and Systems Engineering, Beihang University, Beijing, China. Her research interests include critical phenomena

and phase transition theory.



Md Mahamudur Rahman is currently an Assistant Professor of the Aerospace and Mechanical Engineering Department at the University of Texas at El Paso (UTEP). Prior to joining at UTEP in 2018, he has worked as a Postdoctoral Associate at Massachusetts Institute of Technology. He received his Ph.D. in Mechanical Engineering from

Drexel University in 2016. He has 2 published patents and coauthored 11 journal articles and 58 conference publications and presentations. He is currently working on surface engineering and advanced diagnostics of interfacial phenomena, fluid dynamics, and heat transfer, in-situ resource utilization, hypersonic systems, and digital engineering.



Matteo Bucci is an Associate Professor in the Nuclear Science and Engineering Department at the Massachusetts Institute of Technology. His research interests include the development of high-resolution nonintrusive diagnostics for phase-change studies, boiling heat transfer for nuclear reactors, electronic cooling, and space propulsion

applications, surface engineering, critical phenomena and phase transitions, and machine learning.

References

- C. Li, et al., "Nanostructured copper interfaces for enhanced boiling," Small, vol. 4, no. 8, pp. 1084-1088, Aug. 2008. DOI: 10.1002/smll.200700991.
- R. Chen, et al., "Nanowires for enhanced boiling heat transfer," Nano Lett., vol. 9, no. 2, pp. 548-553, Jan. 2009. DOI: 10.1021/nl8026857.
- M. M. Rahman, E. Ölçeroğlu and M. McCarthy, "Scalable nanomanufacturing of virus-templated coatings for enhanced boiling," Adv. Mater. Interfaces, vol. 1, no. 2, pp. 1300107, Apr. 2014. DOI: 10.1002/admi.201300107.
- M. C. Lu, R. Chen, V. Srinivasan, V. P. Carey and A. Majumdar, "Critical heat flux of pool boiling on Si nanowire array-coated surfaces," Int. J. Heat Mass Transf., vol. 54, no. 25-26, pp. 5359-5367, Dec. 2011. DOI: 10.1016/j.ijheatmasstransfer.2011.08.007.
- H. D. Kim and M. H. Kim, "Effect of nanoparticle deposition on capillary wicking that influences the critical heat flux in nanofluids," Appl. Phys. Lett., vol. 91, no. 1, pp. 014104, Jul. 2007. DOI: 10.1063/1. 2754644.
- S. Li, R. Furberg, M. S. Toprak, B. Palm and M. Muhammed, "Nature-inspired boiling enhancement by novel nanostructured macroporous surfaces," Adv. Funct. Mater., vol. 18, no. 15, pp. 2215-2220, Aug. 2008. DOI: 10.1002/adfm.200701405.
- M. Tetreault-Friend, et al., "Critical heat flux maxima resulting from the controlled morphology of nanoporous hydrophilic surface layers," Appl. Phys. Lett., vol. 108, no. 24, pp. 243102, Jun. 2016. DOI: 10.1063/1.4954012.
- [8] V. Sathyamurthi, H.-S. Ahn, D. Banerjee and S. C. Lau, "Subcooled pool boiling experiments on horizontal heaters coated with carbon nanotubes," J. Heat Transf., vol. 131, no. 7, pp. 071501, Jul. 2009. DOI: 10.1115/1.3000595.
- K. H. Chu, R. Enright and E. N. Wang, "Structured surfaces for enhanced pool boiling heat transfer," Appl. Phys. Lett., vol. 100, no. 24, pp. 241603, Jun. 2012. DOI: 10.1063/1.4724190.
- [10] M. M. Rahman, E. Olceroglu and M. McCarthy, "Role of wickability on the critical heat flux of structured superhydrophilic surfaces," Langmuir, vol. 30, no. 37, pp. 11225-11234, Aug. 2014. DOI: 10.1021/ la5030923.
- N. S. Dhillon, J. Buongiorno and K. K. Varanasi, [11] "Critical heat flux maxima during boiling crisis on textured surfaces," Nat. Commun., vol. 6, no. 1, pp. 1-12, Sep. 2015. DOI: 10.1038/ncomms9247.
- D. E. Kim, S. C. Park, D. I. Yu, M. H. Kim and H. S. Ahn, "Enhanced critical heat flux by capillary driven liquid flow on the well-designed surface," Appl. Phys. Lett., vol. 107, no. 2, pp. 023903, Jul. 2015. DOI: 10.1063/1.4926971.
- B. S. Kim, H. Lee, S. Shin, G. Choi and H. H. Cho, [13] "Interfacial wicking dynamics and its impact on critical heat flux of boiling heat transfer," Appl. Phys.

- Lett., vol. 105, no. 19, pp. 191601, Nov. 2014. DOI: 10.1063/1.4901569.
- A. Zou, D. P. Singh and S. C. Maroo, "Early evapor-[14]ation of microlayer for boiling heat transfer enhancement," Langmuir, vol. 32, no. 42, pp. 10808-10814, Oct. 2016. DOI: 10.1021/acs.langmuir.6b02642.
- [15] H. S. Ahn, H. J. Jo, S. H. Kang and M. H. Kim, "Effect of liquid spreading due to nano/microstructures on the critical heat flux during pool boiling," Appl. Phys. Lett., vol. 98, no. 7, pp. 071908, Feb. 2011. DOI: 10.1063/1.3555430.
- Y. Im, C. Dietz, S. S. Lee and Y. Joshi, "Flower-like [16] CuO nanostructures for enhanced boiling," Nanoscale Microscale Thermophys. Eng., vol. 16, no. 3, pp. 145-153, Jul. 2012. DOI: 10.1080/15567265.2012.678564.
- B. Bon, J. F. Klausner and E. Mckenna, "The hoodoo: a new surface structure for enhanced boiling heat transfer," J. Therm. Sci. Eng. Appl., vol. 5, no. 1, pp. 011003, Mar. 2013. DOI: 10.1115/1.4007439.
- [18] J. Li, et al., "Liquid film-induced critical heat flux enhancement on structured surfaces," Sci. Adv., vol. 7, no. 26, pp. eabg4537, Jun. 2021. DOI: 10.1126/sciadv. abg4537.
- [19] L. Cheng, "Fundamental issues of critical heat flux phenomena during flow boiling in microscale-channels and nucleate pool boiling in confined spaces," Heat Transf. Eng., vol. 34, no. 13, pp. 1016–1043, Oct. 2013. DOI: 10.1080/01457632.2013.763538.
- J. R. Thome, "State-of-the-art overview of boiling [20] and two-phase flows in microchannels," Heat Transf. Eng., vol. 27, no. 9, pp. 4-19, Oct. 2006. DOI: 10. 1080/01457630600845481.
- [21] T. A. Moreira, D. Lee and M. H. Anderson, "Critical heat flux on zircaloy and accident tolerant fuel cladding under prototypical conditions of pressurized and boiling water reactors," Appl. Therm. Eng., vol. 213, pp. 118740, Aug. 2022. DOI: 10.1016/j.applthermaleng.2022.118740.
- G. Y. Su, M. Bucci and P. Sabharwall, Investigations on [22] the Thermal-Hydraulic Behavior of Accident Tolerant Fuel Cladding Materials. Idaho Falls, ID: INL, 2020.
- [23] G. Y. Su, et al., "Wettability and CHF limits of accident-tolerant nuclear fuel cladding materials in light water reactor conditions," Appl. Therm. Eng., vol. 216, pp. 119018, Nov. 2022. DOI: 10.1016/j.applthermaleng.2022.119018.
- Y. V. Polezhaev and S. A. Kovalev, "Modelling heat transfer with boiling on porous structures," Therm. Eng., vol. 37, no. 12, pp. 617-621, 1990.
- [25] S. G. Liter and M. Kaviany, "Pool-boiling CHF enhancement by modulated porous-layer coating: Theory and experiment," Int. J. Heat Mass Transf., vol. 44, no. 22, pp. 4287-4311, Nov. 2001. DOI: 10. 1016/S0017-9310(01)00084-9.
- X. Quan, L. Dong and P. Cheng, "A CHF model for [26] saturated pool boiling on a heated surface with

- micro/nano-scale structures," Int. J. Heat Mass Transf., vol. 76, pp. 452-458, Sep. 2014. DOI: 10. 1016/j.ijheatmasstransfer.2014.04.037.
- [27] R. Li and Z. Huang, "A new CHF model for enhanced pool boiling heat transfer on surfaces with micro-scale roughness," Int. J. Heat Mass Transf., vol. 109, pp. 1084-1093, Jun. 2017. DOI: 10.1016/j. ijheatmasstransfer.2017.02.089.
- L. Zhang, J. H. Seong and M. Bucci, "Percolative scale-free behaviour in the boiling crisis," Phys. Rev. Lett., vol. 122, no. 13, pp. 134501, Apr. 2019. DOI: 10.1103/PhysRevLett.122.134501.
- G.-Y. Su, et al., "Investigation of flow boiling heat transfer and boiling crisis on a rough surface using infrared thermometry," Int. J. Heat Mass Transf., vol. 160, pp. 120134, Oct. 2020. DOI: 10.1016/j.ijheatmasstransfer.2020.120134.
- F. C. Cebeci, Z. Wu, L. Zhai, R. E. Cohen and M. F. Rubner, "Nanoporosity-driven superhydrophilicity: A means to create multifunctional antifogging coatings," Langmuir, vol. 22, no. 6, pp. 2856-2862, Feb. 2006. DOI: 10.1021/la053182p.
- C. K. Wemp and V. P. Carey, "Water wicking and [31] droplet spreading on randomly structured thin nanoporous layers," Langmuir, vol. 33, no. 50, pp. 14513-14525, Nov. 2017. DOI: 10.1021/acs.langmuir.7b03687.
- A. Richenderfer, et al., "Investigation of subcooled [32] flow boiling and CHF using high-resolution diagnostics," Exp. Therm. Fluid Sci., vol. 99, pp. 35-58, Dec. 2018. DOI: 10.1016/j.expthermflusci.2018.07.017.
- M. Bucci, A. Richenderfer, G. Y. Su, T. McKrell and J. Buongiorno, "A mechanistic IR calibration technique for boiling heat transfer investigations," Int. J. Multiph. Flow, vol. 83, pp. 115-127, Jul. 2016. DOI: 10.1016/j.ijmultiphaseflow.2016.03.007.
- [34] M. Ravichandran, et al., "Decrypting the boiling crisis through data-driven exploration of high-resolution infrared thermometry measurements," Appl. Phys. Lett., vol. 118, no. 25, pp. 253903, Jun. 2021. DOI: 10.1063/5.0048391.
- [35] L. Zhang, "A new triggering mechanism of the boiling crisis based on the percolation theory and its implication," Ph.D. dissertation, Dept. Nuclear Science and Engineering. Massachusetts Institute of Technology, Cambridge, MA, 2022.
- [36] S. Mertens and C. Moore, "Continuum percolation thresholds in two dimensions," Phys. Rev. E Stat. Nonlin. Soft. Matter. Phys., vol. 86, no. 6 Pt 1, pp. 061109, Dec. 2012. DOI: 10.1103/PhysRevE.86.061109.
- [37] E. T. Gawlinski and H. E. Stanley, "Continuum percolation in two dimensions: Monte Carlo tests of scaling and universality for non-interacting discs," J. Phys. A Math. Gen., vol. 14, no. 8, pp. L291-L299, Aug. 1981. DOI: 10.1088/0305-4470/14/8/007.